Numerical investigation of a 3D Hybrid High-Order Method for the Indefinite Time-Harmonic Maxwell Problem

Matteo Cicuttin, Christophe Geuzaine

December 5, 2023

Abstract

Hybrid High-Order (HHO) methods are a recently developed class of methods belonging to the broader family of Discontinuous Sketetal methods. Other well known members of the same family are the well-established Hybridizable Discontinuous Galerkin (HDG) method, the nonconforming Virtual Element Method (ncVEM) and the Weak Galerkin (WG) method. HHO provides various valuable assets such as simple construction, support for fully-polyhedral meshes and arbitrary polynomial order, great computational efficiency, physical accuracy and straightforward support for *hp*-refinement. In this work we propose an HHO method for the indefinite time-harmonic Maxwell problem and we evaluate its numerical performance. In addition, we present the validation of the method in two different settings: a resonant cavity with Dirichlet conditions and a parallel plate waveguide problem with a total/scattered field decomposition and a plane-wave boundary condition. Finally, as a realistic application, we demonstrate HHO used on the study of the return loss in a waveguide mode converter.

1 Introduction

Discontinuous Galerkin (DG) methods are very successful discretization methods for the numerical solution of PDEs. Such discretizations rely on discrete spaces made out of broken polynomials, yielding discontinuous discrete solutions. Because of the intrinsic nature of DG methods, they tipically yield a number of degrees of freedom much higher than classical Finite Elements, and this has been a source of criticism about DG. Hybrid methods were therefore introduced to mitigate this issue while retaining all the advantages typical of DG, like full polyhedral support and arbitrary polynomial order. The strategy behind hybrid methods is, very informally, to define some element-local problems and subsequently couple them via face unknowns only: in this way one obtains a global problem posed only in terms of face-based unknowns, contrary to DG which yields a global problem posed in terms of cell-based unknowns. Since unknowns of the global problem are face-based, this class of methods is also known as Discontinuous Skeletal (DS) methods.

A recent development in the family of Discontinuous Skeletal methods is the Hybrid High-Order method (HHO in the following) [27, 26]. The main features of HHO are the approximation of the solution with arbitrary order polynomials, support for fully polyhedral meshes and easy *hp*-refinement. In addition, HHO methods are constructed independently from the geometric dimension and the element shape, allowing fully generic [18] software implementations. In HHO the unknowns are placed both in the cells and on the faces of the mesh, in order to approximate a pair including the primal variable in the cells and its trace on the skeleton. In particular, these unknowns are used by (i) a reconstruction operator, which reconstructs a high-order field in the cell and (ii) by a stabilization operator, which weakly enforces in each mesh cell the matching of the traces of the cell functions with the face unknowns. These two operators are then combined in a local bilinear form which, after local static condensation, is assembled into a global problem posed only on the face unknowns.

HHO methods have been used successfully in several fields of computational mechanics, for example solid mechanics [1, 2, 3], contact problems [11], obstacle problems [19] and fluid mechanics [10, 5]. Recent applications of HHO to acoustic time-domain wave problems can be found in [6] and [7]. To the best of our knowledge however, the only application to electromagnetics, and specifically to magnetostatics, is found in [12].

Bridges and unifying viewpoints between HHO and other DS methods have progressively emerged. One of the most important connections was established in [21], where HHO methods were embedded in the Hybrid Discontinuous Galerkin (HDG) setting [22, 23]. Differently from HHO, HDG approximates a triple including the primal variable, its trace and the dual variable, in addition the analysis of the two methods relies on different theoretical ingredients. Weak Galerkin [39] (WG) methods were bridged to HDG in [24] and therefore are also closely related to HHO. HHO and WG were developed independently, but they share the common point of view of combining a recostruction (called weak gradient in WG) and a stabilization, however HHO employs a more sophisticated stabilization which allows to achieve higher convergence rates. In [21], also a connection to the nonconforming Virtual Element Method [4] was established.

HDG has a rich literature documenting that has been employed successfully in electromagnetics, we cite in particular [13, 34] for magnetostatics and [37, 32, 36, 9, 33] for electromagnetic wave propagation.

In this work we present the construction of an HHO method for the time-harmonic Maxwell problem. As the time-harmonic Maxwell problem is notoriously hard to solve with iterative methods [17], direct solvers are frequently employed, together with domain decomposition techniques. Direct solvers however require huge amounts of memory, and for this reason efficient, high-order discretization techniques are of utmost importance. By employing skeletal (face-based) unknowns, hybrid methods are excellent candidates for this task.

This work is a numerical investigation, and is structured as follows: we first present the construction of the basic method, without providing a full analysis. Subsequently we proceed to a numerical validation on a problem with analytical solution to confirm the expected convergence rates, and we analyze the computational advantage of HHO compared to DG applied to the same problem. In the following sections we devise in the HHO context two tools of practical importance, namely a plane wave source and a Total Field/Scattered Field decomposition. We then proceed to the numerical validation of such tools. We finally use our method to simulate a real-world device and we compare our results with those present in literature.

2 Continuous setting

Let Ω be an open, simply connected subset of $\mathbb{R}^3$. (The method is suitable for any spatial dimension, we take $d = 3$ for conciseness; the restriction to 2D is performed as usual by choosing a TE or TM mode and employing a 2-variate vector for one field and a scalar for the other.) Standard notations will be used in what follows: in particular $L^2(\Omega)$ denotes the Lebesgue space of square integrable functions, $H^1(\Omega)$ the space of functions in $L^2(\Omega)$ whose gradient is square-integrable and $H(\mathrm{curl};\Omega)$ the space of functions in $L^2(\Omega)$ whose curl is square-integrable. In addition, we denote as $H_0(\mathrm{curl};\Omega)$ the subspace of $H(\mathrm{curl};\Omega)$ composed of the functions of $H(\mathrm{curl};\Omega)$ whose trace is zero on $\partial\Omega$. Finally, we denote with $(\cdot,\cdot)_{L^2(\Omega)}$ the inner product on $L^2(\Omega)$ and with $\|\cdot\|_{L^2(\Omega)}$ the corresponding norm.

We consider initially the time-harmonic problem with homogeneous Dirichlet boundary conditions

$$\begin{cases} \nabla \times (\mu^{-1}\nabla \times \boldsymbol{e}) - \omega^2\epsilon\boldsymbol{e} = \boldsymbol{f} & \text{in } \Omega \\ \hat{\boldsymbol{n}} \times \boldsymbol{e} = 0 & \text{on } \partial\Omega \end{cases}, \tag{1}$$

where ω is the angular frequency, μ, ϵ are piecewise constant material parameters, $\boldsymbol{e} \in \mathbb{C}^3$ is the unknown electric field and $\boldsymbol{f} := -i\omega\boldsymbol{j} \in \mathbb{C}^3$ is the divergence-free source current density. Problem (1) is readily translated in weak form: let $V := H_0(\mathrm{curl};\Omega)$; we seek $\boldsymbol{e} \in V$ such that

$$(\mu^{-1}\nabla \times \boldsymbol{e}, \nabla \times \boldsymbol{v})_{\mathbf{L}^2(\Omega)} - \omega^2(\epsilon\boldsymbol{e}, \boldsymbol{v})_{\mathbf{L}^2(\Omega)} = (\boldsymbol{f}, \boldsymbol{v})_{\mathbf{L}^2(\Omega)}, \quad \forall \boldsymbol{v} \in V. \tag{2}$$

3 Discrete setting

Let $\mathcal{M}(\mathcal{T}, \mathcal{F})$ be a polyhedral mesh with $\#\mathcal{T}$ cells and $\#\mathcal{F}$ faces. A generic cell is denoted as $T \in \mathcal{T}$, whereas a generic face as $F \in \mathcal{F}$. Each cell T has diameter h_T and each face F has diameter h_F. The mesh size is defined as $h = \max_{T\in\mathcal{T}} h_T$. We attach to each element T a cell-based vector-valued polynomial $\mathbf{P}_3^k(T)$ and to each one of its n faces $F \in \partial T$ a face-based vector-valued polynomial $\mathbf{P}_2^k(F)$ of degree $k \geqslant 1$. Cell-based polynomials are 3-variate, have values in $\mathbb{C}^3$ and are evaluated directly in the physical element. On the other hand, for each $F \in \partial T$ let H_F be the hyperplane supporting F: face-based polynomials have values in $\mathbb{C}^2$ tangential to H_F and are evaluated using an affine mapping $\mathbf{T}_F : \mathbb{R}^2 \to H_F$. We therefore set

$$\mathbf{P}_2^k(F) := \mathbf{P}_2^k \circ (\mathbf{T}_F^{-1})_{|F}.$$

We remark that an entirely similar procedure can be applied to evaluate face-based functions in the case $d = 2$ (the implementation details are available in [18]); in addition in that case the face-based polynomials will be scalar-valued. Generally speaking, the choice of the tangential face-based polynomial spaces descends directly from the tangential continuity requirement that exists in the $H(\mathrm{curl};\Omega)$ space at the continuous level.

By collecting the cell-based and face-based polynomials attached to an element, the element-local space of degrees of freedom is formed and denoted as

$$\mathsf{U}_T^k := \mathbf{P}_3^k(T) \times \left\{ \bigtimes_{F \in \partial T} \mathbf{P}_2^k(F) \right\}.$$

The elements of U_T^k are denoted as the pairs $\underline{\mathsf{u}}_T := (\mathsf{u}_T, \mathsf{u}_{\partial T})$. In turn, $\mathsf{u}_T \in \mathbf{P}_3^k(T)$ and $\mathsf{u}_{\partial T} = (\mathsf{u}_{F_1}, \ldots, \mathsf{u}_{F_n}), \mathsf{u}_{F_i} \in \mathbf{P}_2^k(F_i)$ are the cell-based and the collection of face-based polynomials respectively (see Figure 1). By collecting all the local polynomials attached to the mesh elements, the global discrete problem space is introduced as

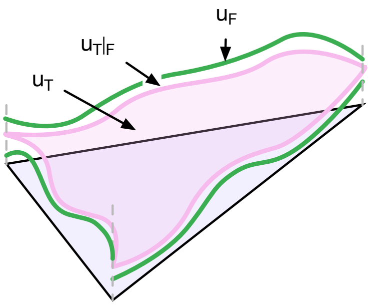

Figure 1: Visual representation of the *local* HHO space: to each mesh element we attach a cell-based function u_T and one face-based function u_F for each face F. Notice that on the vertices the face-based function are discontinuous.

$$\mathsf{U}_h^k := \left\{ \bigtimes_{T \in \mathcal{T}} \mathbf{P}_3^k(T) \right\} \times \left\{ \bigtimes_{F \in \mathcal{F}} \mathbf{P}_2^k(F) \right\},$$

where we remark that the face-based functions are single-valued (see Figure 2). We will denote as $\underline{\mathsf{u}}_h \in \mathsf{U}_h^k$ the elements of the global discrete space and u_h the cell-based part of $\underline{\mathsf{u}}_h$. Homogeneous Dirichlet boundary conditions are enforced strongly by setting to zero the unknowns associated to the boundary faces by considering the subspace of U_h^k

$$\mathsf{U}_{h,0}^k := \left\{ \underline{\mathsf{u}}_h \in \mathsf{U}_h^k \mid \mathsf{u}_F = 0 \quad \forall F \in \partial\Omega \right\}.$$

As the values of the face-based polynomials are vectors tangential to the faces of the elements, this way of imposing the Dirichlet conditions naturally enforces at the discrete level a vanishing tangential component.

3.1 The HHO operators

As the HHO space is composed of hybrid unknowns, we are first faced with the problem of reducing general functions to the HHO space. To this aim, given $\boldsymbol{u} \in L^2(T)$, we denote as $\pi_T^k : L^2(T) \to \mathbf{P}_3^k(T)$ the standard cell-based L^2 projector and $\pi_F^k : L^2(F) \to \mathbf{P}_2^k(F)$ the standard face-based L^2 projector. In addition, we define the tangential trace on the face F as $\gamma_{t,F}(\boldsymbol{u}) := \hat{\boldsymbol{n}}_F \times (\boldsymbol{u} \times \hat{\boldsymbol{n}}_F)$, with $\hat{\boldsymbol{n}}_F$ being the outward normal vector to F. Subsequently, we define the *local reduction operator* $\mathcal{I}_T^k$ such that

$$\mathcal{I}_T^k(\boldsymbol{u}) := (\pi_T^k(\boldsymbol{u}), \pi_{F_1}^k(\gamma_{t,F}(\boldsymbol{u})), \ldots, \pi_{F_n}^k(\gamma_{t,F}(\boldsymbol{u}))).$$

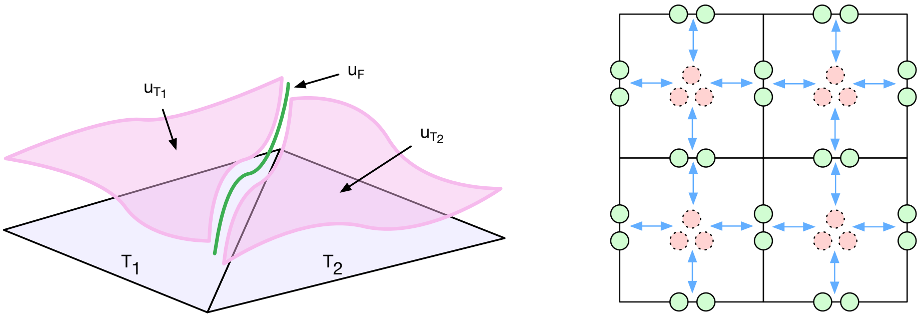

Figure 2: Visual representation of the *global* HHO space. On the left, the result of assembling the local contributions; notice that the face-based functions are single-valued. On the right, the HHO stencil, were we remark that the cell-based unknowns communicate via the face-based unknowns. Cell-based unknowns are eliminated locally via a Schur complement, so they do not appear in the global linear system.

Starting from the last definition, the global reduction operator $\mathcal{I}_h^k$ is obtained trivially by collecting all the contributions of the local operator applied to each mesh element.

The general idea behind skeletal methods is to define some element-local problem which couples to the neighbouring elements via face-based unknowns only. Subsequently, cell-based unknowns are eliminated locally via a Schur complement, allowing to obtain a global transmission problem posed in terms of face unknowns only. In HHO, such local problems are built out of a *reconstruction operator* and a *stabilization* [26]. The reconstruction is typically derived from an integration by parts formula. In the present case we employ the formula

$$(\nabla \times \boldsymbol{u}, \boldsymbol{v})_{\mathbf{L}^2(T)} = (\boldsymbol{u}, \nabla \times \boldsymbol{v})_{\mathbf{L}^2(T)} + (\boldsymbol{u}, \boldsymbol{v} \times \hat{\boldsymbol{n}})_{\mathbf{L}^2(\partial T)}, \tag{3}$$

to derive a *curl reconstruction* [12] operator $\mathcal{C} : \mathsf{U}_T^k \to \mathbf{P}_3^k(T)$. By replacing $\boldsymbol{u}$ with u_T in the volume term on the right-hand side, and $\boldsymbol{u}$ with $\mathsf{u}_{\partial T}$ in the face term, the *curl reconstruction operator* $\mathcal{C}$ is defined to be the solution of the local, well-posed problem

$$(\mathcal{C}\underline{\mathsf{u}}_T, \boldsymbol{v})_{\mathbf{L}^2(T)} := (\mathsf{u}_T, \nabla \times \boldsymbol{v})_{\mathbf{L}^2(T)} + \sum_{F \in \partial T} (\mathsf{u}_F, \boldsymbol{v} \times \hat{\boldsymbol{n}}_F)_{\mathbf{L}^2(F)}, \quad \forall \boldsymbol{v} \in \mathbf{P}_3^k(T). \tag{4}$$

The actual computation of $\mathcal{C}$ requires inverting a mass matrix in each element; this is done just once if a reference element is available (see [20, Chapter 8] for the implementation details). The crucial property of the curl reconstruction operator is that it is polynomially consistent up to polynomial order k: indeed, for all $\boldsymbol{u} \in H(\mathrm{curl}; T)$, by plugging $\mathcal{I}_T^k(\boldsymbol{u})$ in the previous definition we obtain for all $\boldsymbol{v} \in \mathbf{P}_3^k(T)$

$$\begin{aligned}(\mathcal{C}(\mathcal{I}_T^k(\boldsymbol{u})), \boldsymbol{v})_{\mathbf{L}^2(T)} &= (\pi_T^k(\boldsymbol{u}), \nabla \times \boldsymbol{v})_{\mathbf{L}^2(T)} + \sum_{F \in \partial T} (\pi_F^k(\gamma_{t,F}(\boldsymbol{u})), \boldsymbol{v} \times \hat{\boldsymbol{n}}_F)_{\mathbf{L}^2(F)} = \\ &= (\boldsymbol{u}, \nabla \times \boldsymbol{v})_{\mathbf{L}^2(T)} + \sum_{F \in \partial T} (\boldsymbol{u}, \boldsymbol{v} \times \hat{\boldsymbol{n}}_F)_{\mathbf{L}^2(F)} = \\ &= (\nabla \times \boldsymbol{u}, \boldsymbol{v})_{\mathbf{L}^2(T)},\end{aligned}$$

where in the first step the projections were removed owing to the facts that $\nabla \times \boldsymbol{v} \in \mathbf{P}_3^{k-1}(T) \subset \mathbf{P}_3^k(T)$ and $\boldsymbol{v} \times \hat{\boldsymbol{n}}_F \in \mathbf{P}_2^k(F)$, whereas in the second step we applied (3).

Since $\mathcal{C}$ has a nontrivial kernel [20, Chapter 1], we also need a *stabilization* that penalizes the difference between the face-based functions $\mathsf{u}_{\partial T}$ and the tangential component of the cell-based function u_T on ∂T. This ultimately imposes weakly a tangential continuity requirement between elements. Let $\pi_{\gamma,F}^k := \pi_F^k \circ \gamma_{t,F}$. We employ a Lehrenfeld–Schöberl-like stabilization [20, 37], defined as

$$s_T(\underline{\mathsf{u}}_T, \underline{\mathsf{v}}_T) := \sum_{F \in \partial T} \zeta(\mathsf{u}_F - \pi_{\gamma,F}^k(\mathsf{u}_T), \mathsf{v}_F - \pi_{\gamma,F}^k(\mathsf{v}_T))_{\mathbf{L}^2(F)}, \tag{5}$$

where is a scaling factor chosen in order to make the stabilization term dimensionally consistent. In the usual HHO construction one would take $\zeta = (\mu h_T)^{-1}$, however dimensional consistency is achieved also by taking $\zeta = \omega\sqrt{\epsilon/\mu}$ (a similar approach concerning the choice of the penalization parameter is taken in [37] in the HDG context). In the following we will assume $\zeta = \omega\sqrt{\epsilon/\mu}$, but in the validation section we will provide numerical tests comparing the two alternatives.

Notice that the definitions of the reconstruction and the stabilization are *completely element-local*, and this feature will allow us to apply a local Schur complement and eliminate cell-based unknowns during assembly.

With this construction, owing to the polynomial consistency property of $\mathcal{C}$ stated above, we expect a convergence rate of $O(h^{k+1})$ for the L^2-norm of the error $\|\hat{\boldsymbol{e}} - \mathsf{e}_h\|_{\mathbf{L}^2(\Omega)}$, where $\hat{\boldsymbol{e}}$ is such that $\hat{\boldsymbol{e}}_{|T} = \pi_T^k(\boldsymbol{e})$, $\boldsymbol{e}$ is the solution of (1) and $\mathsf{e}_{h|T} = \mathsf{e}_T$ for all $T \in \mathcal{M}$.

3.2 The discrete problem

In order to build the discrete problem we use the curl reconstruction to mimic locally the curl-curl term of (2). We collect this term alongside with the stabilization and the discrete equivalent of the mass term of (2) plus the right-hand side in the bilinear form $a_T : \mathsf{U}_T^k \times \mathsf{U}_T^k \to \mathbb{R}$ and linear form $l_T : \mathsf{U}_T^k \to \mathbb{R}$ as

$$\begin{aligned}
a_T(\underline{\mathsf{e}}_T, \underline{\mathsf{v}}_T) &:= \mu^{-1}(\mathcal{C}\underline{\mathsf{e}}_T, \mathcal{C}\underline{\mathsf{v}}_T)_{\mathbf{L}^2(T)} + s_T(\underline{\mathsf{e}}_T, \underline{\mathsf{v}}_T) - \omega^2\epsilon(\mathsf{e}_T, \mathsf{v}_T)_{\mathbf{L}^2(T)}, \\
l_T(\underline{\mathsf{v}}_T) &:= (\boldsymbol{f}, \mathsf{v}_T)_{\mathbf{L}^2(T)},
\end{aligned}$$

where we remark that the mass term $(\mathsf{e}_T, \mathsf{v}_T)_{\mathbf{L}^2(T)}$ is purely cell-based and the source $\boldsymbol{f}$ is tested only against cell-based basis functions. Static condensation is applied locally to eliminate cell-based DOFs; we refer the reader to [18] for the details. The global problem is obtained by a standard finite element assembly of the bilinear form $a_h(\underline{\mathsf{e}}_h, \underline{\mathsf{v}}_h) : \mathsf{U}_{h,0}^k \times \mathsf{U}_{h,0}^k \to \mathbb{R}$ and the linear form $l_h(\underline{\mathsf{v}}_h) : \mathsf{U}_{h,0}^k \to \mathbb{R}$

$$\begin{aligned}
a_h(\underline{\mathsf{e}}_h, \underline{\mathsf{v}}_h) &:= \sum_{T \in \mathcal{T}} a_T(\mathsf{L}_T\underline{\mathsf{e}}_h, \mathsf{L}_T\underline{\mathsf{v}}_h), \\
l_h(\underline{\mathsf{v}}_h) &:= \sum_{T \in \mathcal{T}} l_T(\mathsf{L}_T\underline{\mathsf{v}}_h),
\end{aligned}$$

where L_T is the classical global-to-local face numbering mapping. We finally solve the global discrete problem of finding $\underline{\mathsf{e}}_h \in \mathsf{U}^k_{h,0}$ such that

$$a_h(\underline{\mathsf{e}}_h, \underline{\mathsf{v}}_h) = l_h(\underline{\mathsf{v}}_h) \quad \forall \underline{\mathsf{v}}_T \in \mathsf{U}^k_{h,0}.$$

3.3 Numerical validation

The described HHO method is implemented in the open-source numerical library DiSk++ (`https://github.com/wareHHOuse/diskpp`). The numerical validation is done on a resonant cavity problem in the domain $[0,1]^3$. The RHS is chosen to obtain the solution $\boldsymbol{e} = (0, 0, sin(\omega x) sin(\omega y))^T$ with $\omega = \pi$ and $\nu = \epsilon = 1$. The objective of the validation is to verify that the method converges with the expected rates and to assess its computational cost in comparison with a classical Symmetric Interior Penalty Discontinuous Galerkin (SIP-DG) discretization [30]. The linear systems obtained from the HHO and SIP-DG discretizations are solved using the PARDISO linear solver found in the Intel MKL library.

The convergence rates and the computational cost of the matrix factorization are summarized in Figure 3. The error convergence rate in L^2-norm results are verified to be $O(h^{k+1})$, as expected. In addition, the computational cost of HHO results to be much lower than that of SIP-DG. HHO being a skeletal discretization, the number of DOFs of the global system grows as $\mathcal{O}(\#\mathcal{F} \cdot k^{d-1})$, compared to $\mathcal{O}(\#\mathcal{T} \cdot k^d)$ in SIP-DG. As such, especially at high polynomial order and on meshes composed mainly of “standard” elements (tetrahedra or hexahedra), HHO is expected to perform much better than SIP-DG. Tables 1 and 2 provide additional confirmation to that expectation. Table 1 reports the number of operations done by PARDISO when deployed on the linear systems obtained from the discretization of the test problem with a tetrahedral mesh of 3072 elements. In Table 2, on the other hand, we report the computational

Table 1: Computational cost comparison between HHO vs. SIP-DG on a tetrahedral mesh of 3072 elements.

	HHO		SIP-DG	
Degree	Memory	Mflops	Memory	Mflops
k=1	0.5 Gb	8.723	0.3 Gb	20.040
k=2	0.9 Gb	66.759	2.4 Gb	313.133
k=3	2.6 Gb	309.072	9.3 Gb	2.560.647

Table 2: Cost comparison between HHO vs. SIP-DG on a polyhedral mesh of 1210 elements (DBLS10 mesh of the FVCA6 benchmark).

	HHO		SIP-DG	
Degree	Memory	Mflops	Memory	Mflops
k=1	0.4 Gb	16.264	0.3 Gb	12.646
k=2	1.4 Gb	130.122	1.6 Gb	211.267
k=3	3.7 Gb	584.182	6.2 Gb	1.690.146
k=4	8.6 Gb	1.971.620	18.5 Gb	8.539.361

advantage of HHO on the DBLS10 polyhedral mesh of the FVCA6 benchmark [28]. As expected the HHO advantage, especially at low order, is slightly lower than in the tetrahedral case.

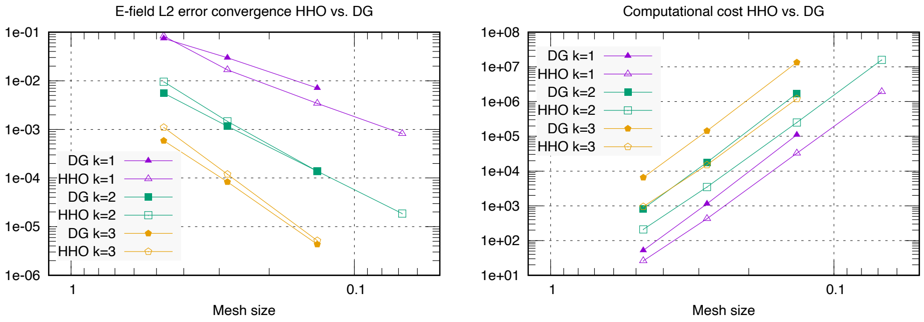

Figure 3: On the left panel, the L^2-norm convergence rates of HHO compared to SIP-DG on tetrahedral meshes. On the right panel, the number of floating poing operations done by the linear solver. HHO error is slightly higher than DG error, however at higher polynomial orders HHO is one order of magnitude cheaper than SIP-DG.

We conclude the computational performance evaluation with Table 3, in which we show the cost of HHO to attain a certain fixed error while varying mesh size and polynomial order.

Table 3: Computational effort required for HHO to attain roughly the same L^2-norm error at different polynomial orders.

Mesh h	k	Error	Mflops	DOFs	Memory
0.103843	2	3.56e-5	4089984	571392	11.7 Gb
0.207712	3	1.38e-5	309072	115200	2.6 Gb
0.415631	4	1.98e-5	16287	20160	0.5 Gb
0.832917	6	1.24e-5	1265	4032	0.1 Gb

We would like to stress the fact that HHO is one of the many possible points of view over the hybridization of the classical DG method, others being the already mentioned HDG, ncVEM and WG. Despite the different points of view however, bridges have been established between HHO, HDG, ncVEM and WG and indeed they all yield a skeleton-based discrete problem. This fact suggests that all these discretizations should obtain similar computational advantages over DG. We would also like to remark that the DG assembly should, in general, be a little less expensive, as hybrid methods require the solution of a small local problem in each mesh element. However, as our goal is to decrease the memory usage during the solution phase, we consider that a slightly heavier assembly process is of secondary importance.

4 Additional boundary conditions and field sources

Practical applications frequently require specialized treatment of boundaries and sources. In this section we discuss a plane wave boundary condition [14] and a total field/scattered field decomposition, and in particular we detail their realization in the HHO framework. The former is basically a non-homogeneous Robin condition and is used either to impose an active plane wave source or a passive absorbing boundary condition on a boundary $\Gamma_Z \subset \partial\Omega$. The latter is a common technique to impose sources in the FDTD method and study reflection coefficients; it has been successfully used also in FETD (Finite-Element Time-Domain) [38] and other frequency domain methods [16, 35].

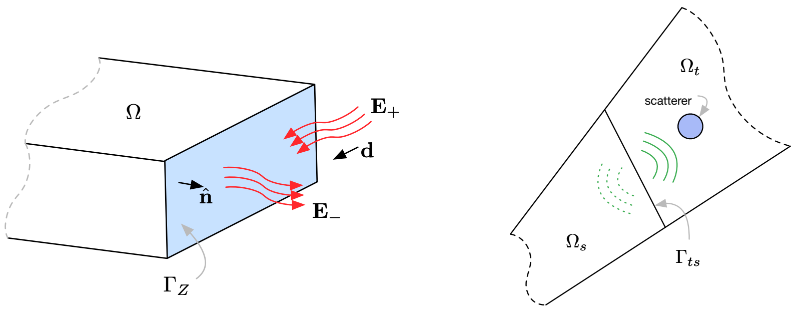

(a) (b)

Figure 4: In the left panel, the fields, vectors and surfaces involved in the definition of the plane wave boundary condition. In the right panel, the domains and interfaces involved in the TF/SF decomposition. On Ω_t the full field is computed, whereas in Ω_s only the reflections produced in Ω_t are computed.

4.1 Plane wave boundary condition

With reference to Figure 4a, let $\boldsymbol{E}_+$ denote the complex amplitude of the known electric field of a wave entering Ω through Γ_Z and propagating in direction $\boldsymbol{d}$. Similarly, let $\boldsymbol{E}_-$ denote the complex amplitude of the unknown electric field of a wave exiting Ω through Γ_Z and propagating in direction $\hat{\boldsymbol{n}}$. In addition, let $\kappa^2 = \omega^2\mu\epsilon$. In this setting, the total electric field on Γ_Z at the point $\boldsymbol{x} \in \Gamma_Z$ is given by

$$\boldsymbol{e}(\boldsymbol{x}) = \boldsymbol{E}_+ e^{-i\kappa(\boldsymbol{d}\cdot\boldsymbol{x})} + \boldsymbol{E}_- e^{-i\kappa(\boldsymbol{n}\cdot\boldsymbol{x})}. \tag{6}$$

By taking the curl of (6) and applying the vector calculus identity $\nabla \times (\psi \boldsymbol{A}) = \psi(\nabla \times \boldsymbol{A}) + \nabla\psi \times \boldsymbol{A}$, we obtain

$$\nabla \times \boldsymbol{e} = -i\kappa \left(\boldsymbol{d} \times \boldsymbol{E}_+ e^{-i\kappa(\boldsymbol{d}\cdot\boldsymbol{x})} + \hat{\boldsymbol{n}} \times \boldsymbol{E}_- e^{-i\kappa(\hat{\boldsymbol{n}}\cdot\boldsymbol{x})} \right). \tag{7}$$

We now post-multiply by $\hat{\boldsymbol{n}}$ and replace (6) in the result to obtain

$$(\nabla \times \boldsymbol{e}) \times \hat{\boldsymbol{n}} + i\kappa\left(\hat{\boldsymbol{n}} \times (\boldsymbol{e} \times \hat{\boldsymbol{n}})\right) = i\kappa \left((\hat{\boldsymbol{n}} - \boldsymbol{d}) \times \boldsymbol{E}_+ e^{-i\kappa(\boldsymbol{d}\cdot\boldsymbol{x})} \right) \times \hat{\boldsymbol{n}}. \tag{8}$$

By pre-multiplying both sides of (8) by μ^{-1} we can make the wave admittance $Y = \sqrt{\epsilon/\mu}$ explicit

$$(\mu^{-1}\nabla \times \boldsymbol{e}) \times \hat{\boldsymbol{n}} + i\omega Y \boldsymbol{e}_t = i\omega Y \boldsymbol{e}_t^+(\boldsymbol{d}), \tag{9}$$

where we replaced the two double-cross-product terms of (8) with the shorthands $\boldsymbol{e}_t := \hat{\boldsymbol{n}} \times (\boldsymbol{e} \times \hat{\boldsymbol{n}})$ and $\boldsymbol{e}_t^+(\boldsymbol{d}) := \left((\hat{\boldsymbol{n}} - \boldsymbol{d}) \times \boldsymbol{E}_+ e^{-i\kappa(\boldsymbol{d}\cdot\boldsymbol{x})}\right) \times \hat{\boldsymbol{n}}$ respectively. The condition just obtained goes under the name of *plane wave* condition. It can then be incorporated in the strong form Maxwell problem as

$$\begin{cases} \nabla \times (\mu^{-1}\nabla \times \boldsymbol{e}) - \omega^2\epsilon\boldsymbol{e} = -i\omega\boldsymbol{j} & \text{in } \Omega \\ \hat{\boldsymbol{n}} \times \boldsymbol{e} = 0 & \text{on } \Gamma_D \\ (\mu^{-1}\nabla \times \boldsymbol{e}) \times \hat{\boldsymbol{n}} + i\omega Y\boldsymbol{e}_t = i\omega Y\boldsymbol{e}_t^+(\boldsymbol{d}) & \text{on } \Gamma_Z \end{cases}, \tag{10}$$

where $\boldsymbol{j}$ is the divergence-free current density, $\Gamma_Z \cup \Gamma_D = \partial\Omega$ and $\Gamma_Z \cap \Gamma_D = \varnothing$. Let $H_i(\text{curl};\Omega)$ be the space defined as

$$H_i(\text{curl};\Omega) := \{\boldsymbol{\phi} \in H(\text{curl};\Omega) \mid \gamma_{t,\Gamma_Z}(\boldsymbol{\phi}) \in L^2(\Gamma_Z) \text{ on } \Gamma_Z, \hat{\boldsymbol{n}} \times \boldsymbol{\phi} = 0 \text{ on } \Gamma_D\}.$$

With standard manipulations, Problem (10) is translated to weak form, where we look for $\boldsymbol{e} \in H_i(\text{curl};\Omega)$ such that the expression

$$\begin{aligned} \mu^{-1}(\nabla \times \boldsymbol{e}, \nabla \times \boldsymbol{v})_{\mathbf{L}^2(\Omega)} - \omega^2\epsilon(\boldsymbol{e}, \boldsymbol{v})_{\mathbf{L}^2(\Omega)} + i\omega Y(\boldsymbol{e}_t, \boldsymbol{v})_{\mathbf{L}^2(\Gamma_Z)} &= \\ = i\omega Y(\boldsymbol{e}_t^+(\boldsymbol{d}), \boldsymbol{v})_{\mathbf{L}^2(\Gamma_Z)} - i\omega(\boldsymbol{j}, \boldsymbol{v})_{\mathbf{L}^2(\Omega)}&, \end{aligned} \tag{11}$$

holds for all the test functions $\boldsymbol{v} \in H_i(\text{curl};\Omega)$. In the local HHO bilinear forms, the new impedance and boundary source terms appearing in (11) translate to a face-based mass matrix and a face-based right-hand side respectively, as in

$$\begin{aligned} a_T(\underline{\mathsf{e}}_T, \underline{\mathsf{v}}_T) &:= \mu^{-1}(\mathcal{C}\underline{\mathsf{e}}_T, \mathcal{C}\underline{\mathsf{v}}_T)_{\mathbf{L}^2(T)} + s_T(\underline{\mathsf{e}}_T, \underline{\mathsf{v}}_T) - \omega^2\epsilon(\mathsf{e}_T, \mathsf{v}_T)_{\mathbf{L}^2(T)} \\ &\quad + \sum_{F \in \partial T \cap \Gamma_Z} i\omega Y(\mathsf{u}_F, \mathsf{v}_F)_{\mathbf{L}^2(F)} \\ l_T(\underline{\mathsf{v}}_T) &:= \sum_{F \in \partial T \cap \Gamma_Z} i\omega Y(\boldsymbol{e}_t^+(\boldsymbol{d})), \mathsf{v}_F)_{\mathbf{L}^2(F)} - i\omega(\boldsymbol{j}, \mathsf{v}_T)_{\mathbf{L}^2(T)} \end{aligned}$$

The global system assembly procedure remains unchanged, except for the discrete global space of the problem, which is now

$$\mathsf{U}_{h,i}^k := \left\{\underline{\mathsf{u}}_h \in \mathsf{U}_h^k \mid \mathsf{u}_F = 0 \quad \forall F \in \Gamma_D\right\}.$$

4.2 Total field/scattered field decomposition

The total/scattered field (TF/SF) decomposition is a technique [35, 16, Section 3.2] used to place surface field sources inside a computational domain, and it is usually employed to study the reflection characteristics of a device (e.g. the return loss).

A TF/SF decomposition splits the computational domain Ω in two partitions Ω_t and Ω_s such that $\Omega_t \cup \Omega_s = \Omega$, $\Omega_t \cap \Omega_s = \varnothing$ and $\overline{\Omega_t} \cap \overline{\Omega_s} = \Gamma_{ts}$ (see Figure 4b). The field in Ω_s is then the result of the scatterings occurring in Ω_t, minus the source applied on the interface Γ_{ts} and radiating into Ω_t. For simplicity in this work Γ_{ts} is fitted to the mesh; HHO supports also unfitted interfaces as demonstrated in [8] for elliptic problems and in [5] for the Stokes problem.

In our setting, we consider the source applied on Γ_{ts} to be a plane wave with electric field $\tilde{\boldsymbol{e}} : \Gamma_{ts} \to \mathbb{C}^3$ and magnetic field $\tilde{\boldsymbol{h}} : \Gamma_{ts} \to \mathbb{C}^3$. Therefore, denoting with Y the wave admittance, it holds

$$\tilde{\boldsymbol{h}} \times \hat{\boldsymbol{n}} = Y\hat{\boldsymbol{n}} \times (\tilde{\boldsymbol{e}} \times \hat{\boldsymbol{n}}).$$

By setting $\boldsymbol{s}_D := \hat{\boldsymbol{n}} \times (\tilde{\boldsymbol{e}} \times \hat{\boldsymbol{n}})$ and invoking the Faraday-Neumann law on the left hand side of the above equation, we define $\boldsymbol{s}_N := -i\omega Y \boldsymbol{s}_D$. The TF/SF decomposition can therefore be formulated as the problem

$$\begin{cases} \nabla \times (\mu^{-1} \nabla \times \boldsymbol{e}) - \omega^2 \epsilon \boldsymbol{e} = 0 & \text{in } \Omega \\ [\![\hat{\boldsymbol{n}} \times \boldsymbol{e} \times \hat{\boldsymbol{n}}]\!] = \boldsymbol{s}_D & \text{on } \Gamma_{ts} \\ [\![(\mu^{-1} \nabla \times \boldsymbol{e}) \times \hat{\boldsymbol{n}}]\!] = \boldsymbol{s}_N & \text{on } \Gamma_{ts} \\ \hat{\boldsymbol{n}} \times \boldsymbol{e} = 0 & \text{on } \partial\Omega \end{cases}, \tag{12}$$

where we denote with $[\![\cdot]\!]$ the standard jump operator and the normal is oriented towards the total field part on Γ_{ts} and outwards on $\partial\Omega$.

The discontinuous skeletal nature of the HHO method makes particularly convenient to impose the jump conditions on Γ_{ts}: only the Dirichlet jump requires a slightly specialized treatment, the Neumann jump is handled as if it were a regular Neumann condition on a domain boundary.

Let T^t and T^s be two elements (we use triangles for illustration purposes, the reasoning applies to all polygons/polyhedra) sharing a face on Γ_{ts} (Figure 5). The faces of T^t are denoted as F_1^t, F_2^t, F_Γ^t; similarly the faces of T^s are denoted as F_1^s, F_2^s, F_Γ^s. The faces with the subscript Γ lie on Γ_{ts} and, from the point of view of the global discrete problem, $F_\Gamma^t = F_\Gamma^s$. The associated local unknowns are denoted as follows: for T^t we have the cell-based contribution e_{T^t} and the face-based contributions $\mathsf{e}_{F_1^t}$, $\mathsf{e}_{F_2^t}$ and $\mathsf{e}_{F_\Gamma^t}$, whereas on T^s we have the cell-based contribution e_{T^s} and the face-based contributions $\mathsf{e}_{F_1^s}$, $\mathsf{e}_{F_2^s}$ and $\mathsf{e}_{F_\Gamma^s}$.

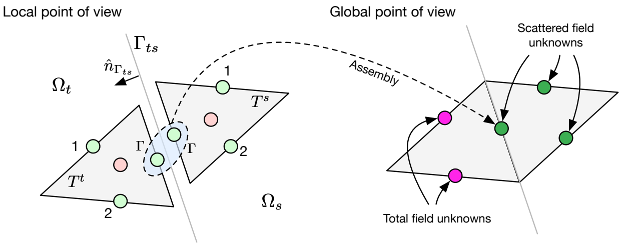

Figure 5: On the left, the unknowns of two elements across the TF/SF boundary. The two face-based values across the interface marked Γ (dashed circle) contribute to the same unknown of the global problem. On the right, the two elements after assembly: in our setting we consider that unknowns on Γ_{ts} are scattered field unknowns.

The face-based unknowns of the global discrete problem, as already mentioned, are single-valued and the face-based quantities $\mathsf{e}_{F_\Gamma^t}$ and $\mathsf{e}_{F_\Gamma^s}$ contribute to the same global unknown (Figure 5). Therefore, it must be chosen whether the global unknown on Γ_{ts} represents a total field or a scattered field quantity. In this work, we chose the latter.

From a local point of view the previous choice allows to reason as follows. First, let $\boldsymbol{e}_s := \boldsymbol{e}_{|\Omega_s}$ and $\boldsymbol{e}_t := \boldsymbol{e}_{|\Omega_t}$, so the Dirichlet jump condition of (12) is rewritten as $\hat{\boldsymbol{n}}_{\Gamma_{ts}} \times \boldsymbol{e}_t \times \hat{\boldsymbol{n}}_{\Gamma_{ts}} = \hat{\boldsymbol{n}}_{\Gamma_{ts}} \times \boldsymbol{e}_s \times \hat{\boldsymbol{n}}_{\Gamma_{ts}} + \boldsymbol{s}_D$ on Γ_{ts}. Then, as at the discrete level the face-based degrees of freedom are vectors tangential to the face itself, the discrete equivalent on T^t of the previous relation is $\mathsf{e}_{F_\Gamma^t} = \mathsf{e}_{F_\Gamma^s} + \mathsf{s}_D$, where $\mathsf{s}_D = \pi^k_{F^t_\Gamma}(\gamma_{t,F}(\boldsymbol{s}_D))$. On T^t we thus define the local reconstruction as

$$\begin{aligned}
(\mathcal{C}\underline{\mathsf{e}}_{T^t}, \boldsymbol{v})_{\mathbf{L}^2(T^t)} &:= (\mathsf{e}_{T^t}, \nabla \times \boldsymbol{v})_{\mathbf{L}^2(T^t)} + \sum_{i \in \{1,2,\Gamma\}} (\mathsf{e}_{F^t_i}, \boldsymbol{v} \times \hat{\boldsymbol{n}}_{F^t_i})_{\mathbf{L}^2(F^t_i)} \\
&= (\mathsf{e}_{T^t}, \nabla \times \boldsymbol{v})_{\mathbf{L}^2(T^t)} \quad + \sum_{i \in \{1,2\}} (\mathsf{e}_{F^t_i}, \boldsymbol{v} \times \hat{\boldsymbol{n}}_{F^t_i})_{\mathbf{L}^2(F^t_i)} \\
&\qquad + (\mathsf{e}_{F^s_\Gamma} + \mathsf{s}_D, \boldsymbol{v} \times \hat{\boldsymbol{n}}_{F^t_\Gamma})_{\mathbf{L}^2(F^t_\Gamma)}.
\end{aligned} \tag{13}$$

Plainly speaking, the only difference with the standard reconstruction (4) is that the face term on F^t_Γ has been modified to take into account both the unknown scattered field contribution and the known source contribution. On the other hand, the reconstruction operator on T^s remains unchanged, as the unknown on F^s_Γ is already a scattered field quantity.

From the above considerations, the local discrete bilinear form and linear form on T^t are readily derived as

$$a^{ts}_T(\underline{\mathsf{e}}^\flat_T, \underline{\mathsf{v}}_T) := \mu^{-1}(\mathcal{C}\underline{\mathsf{e}}^\flat_T, \mathcal{C}\underline{\mathsf{v}}_T)_{\mathbf{L}^2(T)} - \omega^2\epsilon(\mathsf{e}_T, \mathsf{v}_T)_{\mathbf{L}^2(T)} + s_T(\underline{\mathsf{e}}^\flat_T, \underline{\mathsf{v}}_T), \tag{14}$$

$$l^{ts}_T(\underline{\mathsf{v}}_T) := -a^{ts}_T(\underline{\mathsf{s}}_D, \underline{\mathsf{v}}_T) + (\boldsymbol{s}_N, \mathsf{v}_{F^t_\Gamma})_{\mathbf{L}^2(F^t_\Gamma)}, \tag{15}$$

where $\underline{\mathsf{s}}_D := \mathcal{I}^k_T(\boldsymbol{s}_D)$ and the subscript $\flat$ indicates that some face-based contributions in $\underline{\mathsf{e}}^\flat_T$ are on Γ_{ts} and therefore are scattered field quantities.

From an implementation point of view, the TF/SF decomposition requires special handling of only the elements of Ω_t touching Γ_{ts}. In particular, on those elements only additional contributions on the right-hand side arise. The left-hand side is identical to the non-TF/SF case.

5 Numerical validation of additional conditions and sources

In this section we provide some validation results about the impedance boundary condition and the total field/scattered field decomposition developed for the HHO framework. To this aim, we set up a parallel-plate waveguide problem whose analytical solution can be readily obtained by basic transmission line theory considerations [25]. In particular, we will consider the propagation of an electromagnetic wave through a material discontinuity with various degrees of impedance mismatch. In this setting, we study the convergence to the analytical solution and the convergence of the return loss measured at the source.

5.1 Detailed validation setup

We consider the domain $\Omega = (0, 0.1) \times (0, 0.1) \times (-0.2, 2)$. Additionally, we subdivide Ω along the coordinate z in three subregions Ω_3, Ω_1 and Ω_2 (Figure 6). The region Ω_3 extends in the interval $(-0.2, 0)$ along z and is a scattered field region, whereas Ω_1 and Ω_2 are both total field region which cover the z intervals $(0, 1)$ and $(1, 2)$ respectively. On the boundaries parallel to the xz-plane a homogeneous Dirichlet boundary condition ($\hat{\boldsymbol{n}} \times \boldsymbol{e} = 0$) is applied, whereas on the boundaries parallel to the yz-plane a homogeneous Neumann boundary condition ($\boldsymbol{h} \times \hat{\boldsymbol{n}} = 0$) is applied. A plane wave source of amplitude $\boldsymbol{E}_0 =$

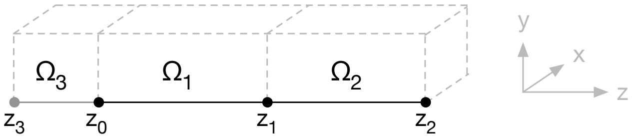

Figure 6: Computational domain used to setup a parallel-plate waveguide for the validation of the impedance boundary condition and the TF/SF decomposition.

$(0,1,0)^T$ is applied via (14-15) in the plane at $z = z_0 = 0$, whereas on the planes $z = z_3 = -0.2$ and $z = z_2 = 2$ an impedance boundary condition is imposed. In the regions Ω_3 and Ω_1 the material parameters are set to $\epsilon = \epsilon_0$ and $\mu = \mu_0$, simulating free space. On the other hand, in Ω_2 we set $\epsilon = \epsilon_r\epsilon_0$ and $\mu = \mu_0$ in order to obtain a material discontinuity on the plane at $z = z_1 = 1$. In turn, this gives on the same plane a reflection coefficient γ_{12} and a transmission coefficient τ_{12} (seen from 1 to 2).

In this setting, the reference solution can be defined piecewise by resorting to the standard transmission line theory (Figure 7). We start with Ω_1 by observing that there will be a forward wave due to the excitation at z_0, and a backward wave reflected by the material discontinuity at z_1. The expression of the forward wave is easily deduced to be $\boldsymbol{E}_0 e^{-i\kappa_1(z-z_0)}$; in addition we notice that at the point z_1 the phase is $\phi_1 = -i\kappa_1(z_1 - z_0)$. Subsequently, by using the last observation and the fact that at z_1 the reflection coefficient is γ_{12}, we deduce that the backward wave originating at z_1 can be written as $\boldsymbol{E}_0\,\gamma_{12}\,e^{i\kappa_1(z-z_1)}e^{\phi_1}$. Concerning Ω_2, as the domain is terminated by a matched impedance condition, we expect only a forward wave with initial amplitude $\boldsymbol{E}_0\,\tau_{12}$ and initial phase ϕ_1. Finally, as Ω_3 is a scattered field region, we expect to see only the backward wave originating at z_1, whose expression was already derived above. The complete, piecewise reference solution can finally be written as follows:

$$\boldsymbol{e}_{\mathrm{ref}}(\boldsymbol{x}) = \begin{cases} \boldsymbol{E}_0\,\gamma_{12}\,e^{i\kappa_1(z-z_1)}e^{\phi_1} & \text{in } \Omega_3 \\ \boldsymbol{E}_0 e^{-i\kappa_1(z-z_0)} + \boldsymbol{E}_0\,\gamma_{12}\,e^{i\kappa_1(z-z_1)}e^{\phi_1} & \text{in } \Omega_1 \\ \boldsymbol{E}_0\,\tau_{12}\,e^{-i\kappa_2(z-z_1)}e^{\phi_1} & \text{in } \Omega_2 \end{cases} \tag{16}$$

5.2 Validation results

For the validation we consider three different situations: an almost matched situation, a situation with a moderate mismatch and one with a severe mismatch. In particular we will consider the values of ϵ_r in Ω_2 reported in Table 4.

Table 4: The parameters of the three situations considered as validation cases. For a given value of ϵ_r, the analytical values of the reflection coefficient, transmission coefficient, return loss in dB and VSWR respectively are reported.

Situation	ϵ_r	γ_{12}	τ_{12}	RL(dB)	VSWR
Almost matched	1.44	-1/11	10/11	-20.8279	1.2:1
Moderate mismatch	4	-1/3	2/3	-9.5424	2:1
Severe mismatch	64	-7/9	2/9	-2.1829	8:1

In the three situations we expect different magnitudes of forward and reflected waves; the analytical solution of the problem is reported in Figure 7.

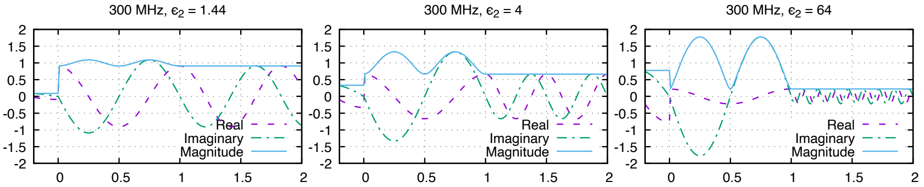

Figure 7: Analytical solution at 300 MHz in the three considered test cases. The symbol ϵ_2 denotes the relative permittivity in the subregion Ω_2 of the testing domain.

We recall [25] that the wave impedance in the domain Ω_i is computed from the material parameters as $Z_i = \sqrt{\mu/\epsilon}$. Given two differents, adjacent domains Ω_i and Ω_j, the reflection and transmission coefficients at the interface from Ω_i to Ω_j are computed as $\gamma_{ij} = \frac{Z_i - Z_j}{Z_i + Z_j}$ and $\tau_{ij} = 2\frac{Z_j}{Z_i + Z_j}$ respectively; the return loss in decibels at at the same interface is computed as $\mathrm{RL(dB)} = 20\log_{10}|\gamma_{ij}|$ and the voltage standing wave ratio as $\mathrm{VSWR} = \frac{1+|\gamma_{ij}|}{1-|\gamma_{ij}|}$. We recall that the return loss is given also by the ratio between the reflected and incident power at a given interface as $RL(dB) = 10\log_{10}(P_{\mathrm{ref}}/P_{\mathrm{fwd}})$. Finally, the power P flowing at a given interface Γ is obtained by evaluating the flux of the Poynting vector [31, Section 5.1] as $P = \int_\Gamma |\boldsymbol{e}|^2/Z d\Gamma$, where Z is the impedance of the domain adjacent to Γ.

The results of the validation are reported in the Figures 8, 9 and 10. We considered polynomials degrees $k = 1$ (top row in the figures) and $k = 2$ (bottom row in the figures) and we ran the computations on a sequence of meshes of size $h \in \{0.16, 0.08, 0.04, 0.02, 0.01\}$. In all cases the error decays with the expected rate ($\mathcal{O}(h^2)$ in the case $k = 1$ and $\mathcal{O}(h^3)$ in the case $k = 2$), see left column of Figures 8, 9 and 10. On the right column of the figures we reported the convergence of the return loss at the interface at z_0; we remark that this computation, especially in the severely mismatched situation, benefits greatly from higher order. In addition, we notice that there is no "direction" in the convergence of the value of the return loss: in some cases the convergence is from above, in some cases from below and in other cases there is an oscillation (getting smaller with smaller h) around the true value. This behaviour is in accordance with what was already observed in [15] in the context of the Discrete Geometric Approach (DGA) method.

6 On the choice of the stabilization parameter

The traditional stabilization of the HHO methods descends directly from the norm associated to the discrete space in use [20, Chapter 1] and employed to prove the stability and convergence of the method. Therefore, according to the HHO theory, one should choose $\zeta := (\mu h_T)^{-1}$ in (5) to achieve dimensional consistency of the stabilization term when material parameters are taken into account as in (2). Taking inspiration from the impedance boundary

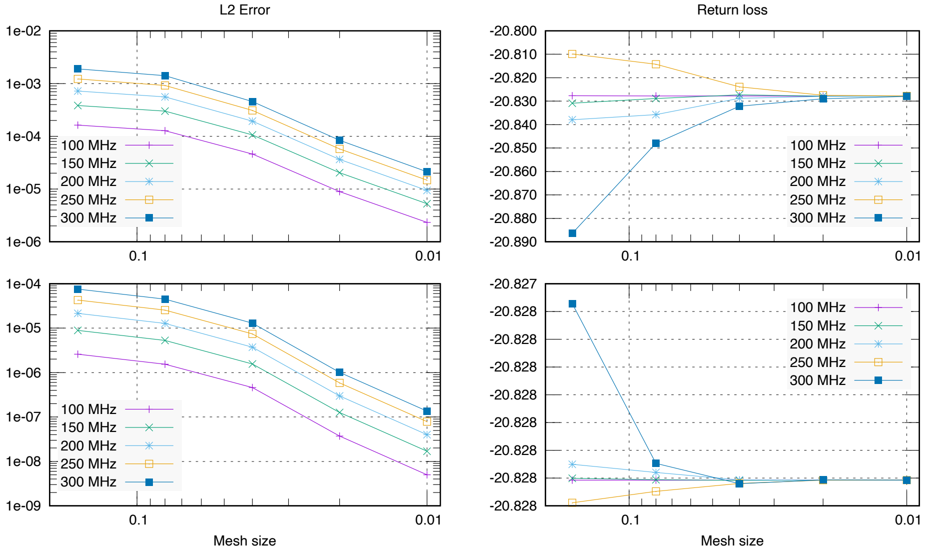

Figure 8: Almost matched (VSWR 1.2:1), on the top row polynomial order $k = 1$ and on the bottom row polynomial order $k = 2$. On the left column the convergence rate to the reference solution is reported, whereas in the right column the convergence of the return loss is depicted.

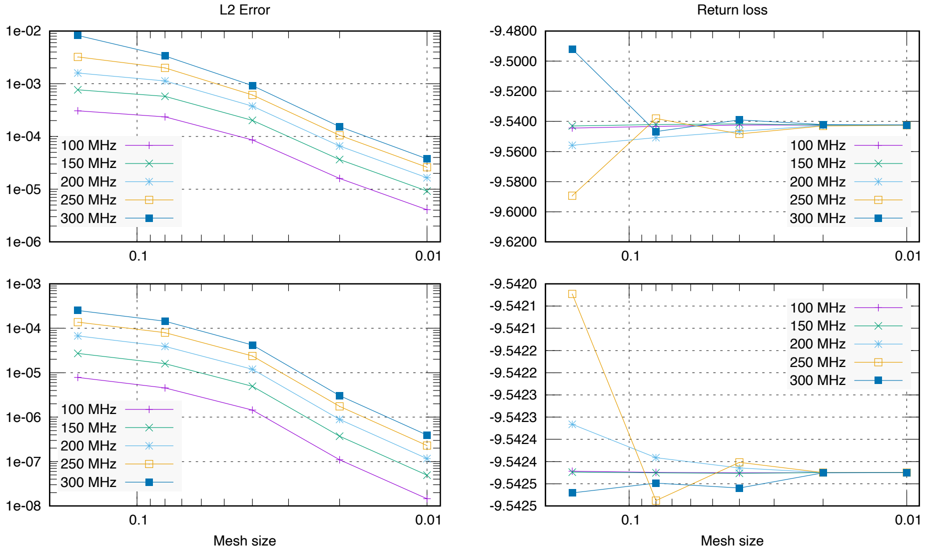

Figure 9: Moderate mismatch (VSWR 2:1), on the top row polynomial order $k = 1$ and on the bottom row polynomial order $k = 2$. On the left column the convergence rate to the reference solution is reported, whereas in the right column the convergence of the return loss is depicted.

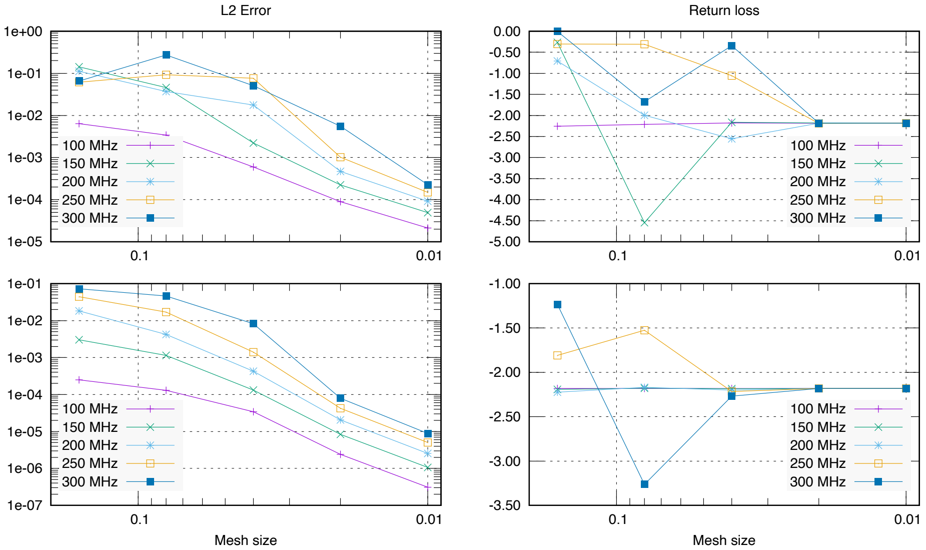

Figure 10: Severe mismatch (VSWR 8:1), on the top row polynomial order $k = 1$ and on the bottom row polynomial order $k = 2$. On the left column the convergence rate to the reference solution is reported, whereas in the right column the convergence of the return loss is depicted.

condition however, one can empirically deduce that also $\zeta := \omega\sqrt{\epsilon/\mu}$ yields a dimensionally-consistent stabilization.

In this section we provide some empirical data about the behaviour of the method using the two different parameters. We will refer to the choice $\zeta := (\mu h_T)^{-1}$ as "standard" and to the choice $\zeta := \omega\sqrt{\epsilon/\mu}$ as "modified".

We ran the validation problem of Section 5 at $f \in \{200, 250, 300\}$ MHz (as the error is the highest) using the two stabilization parameters. In the almost matched case, even if the modified stabilization parameter produces a slightly higher error, the two choiches remain equivalent for practical purposes (Figure 11); for conciseness we report the results only for $k = 1$ as with $k = 2$ the behaviour is comparable.

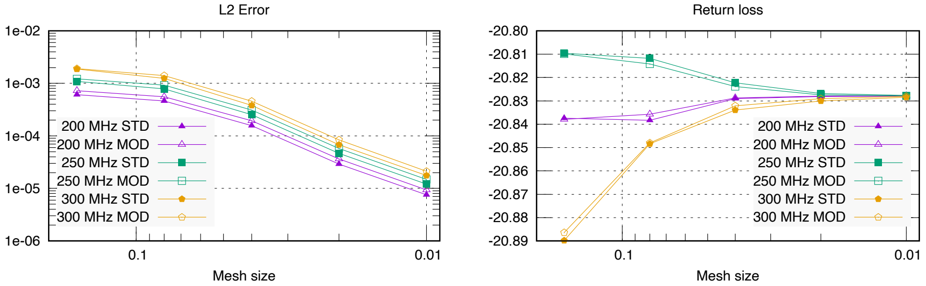

Figure 11: Comparison of the two stabilization parameters in the almost matched case. With the modified parameter, the error is slightly higher, however the two choiches remain essentially equivalent.

In the moderately mismatched case, for which we report the results for $k = 1$

(Figure 12), we observe that the error behaviour is improved only for the coarsest meshes; on the finer meshes the choices are equivalent up to some slight increase of the error.

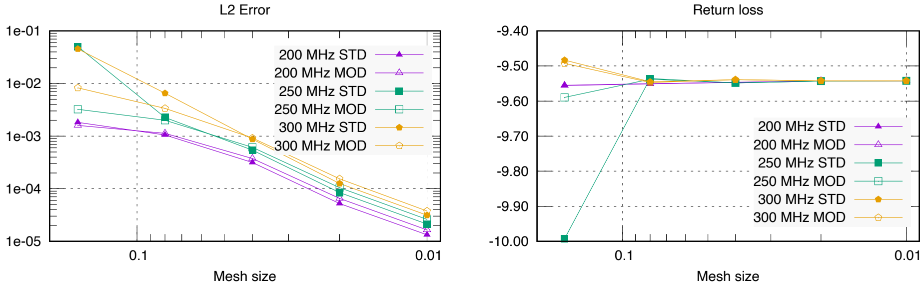

Figure 12: Comparison of the two stabilization parameters in the moderately mismatched case. With the modified stabilization, on the coarse meshes the method attains a lower error.

In the severely mismatched case we observe that the modified stabilization parameter greatly improves the error behaviour of the method in case $k = 1$ but especially in the case $k = 2$; we report both in Figure 13.

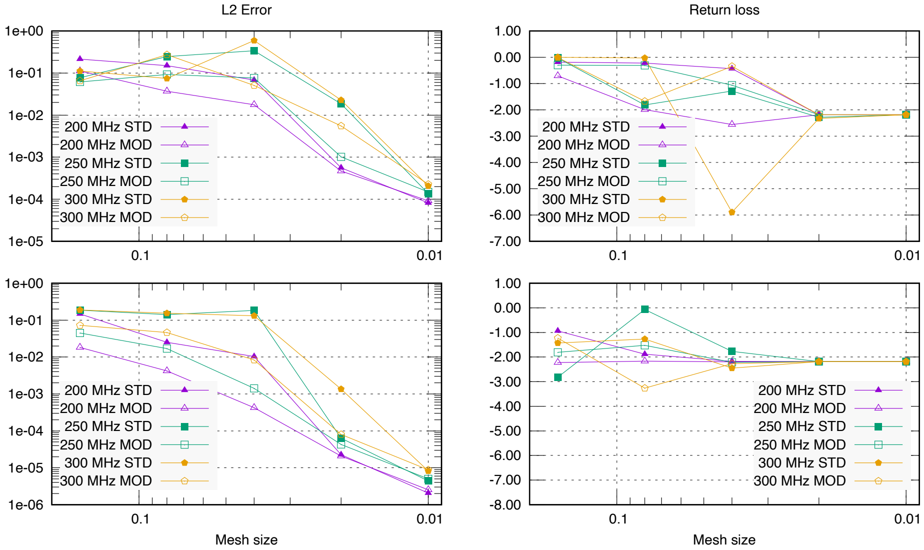

Figure 13: Comparison of the two stabilization parameters in the severely mismatched case. With the modified stabilization the method attains a lower error in all but the last mesh of the test sequence.

To conclude the comparison between the standard and the modified stabilization parameters, we evaluated the error for the two cases along the line from $(0.05, 0.05, -0.2)$ to $(0.05, 0.05, 2)$, in order to determine if, in the cases where the modified parameter yielded a better error, the improvements were localized or global. In general we observed global improvements, in Figure 14 we report the comparison in the moderately mismatched case, $h = 0.16, k = 1, f = 300$ MHz and the severely mismatched case, $h = 0.04, k = 1, f = 300$ MHz.

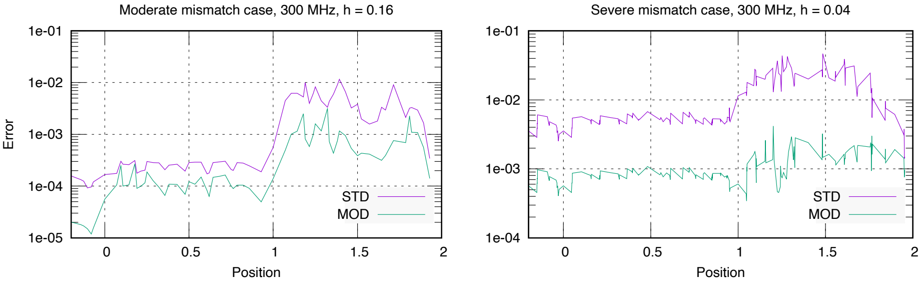

Figure 14: Error of the method with the two stabilization parameters vs. position inside the domain. The distribution of the error appears similar for the two stabilizations.

7 Study of a TE_{10} to TE_{20} mode converter

To conclude the numerical evaluation of the proposed HHO method, we consider a realistic test case of a waveguide mode converter. In this setting a waveguide is a hollow metallic pipe used to transport electromagnetic energy from a generator to a load (for example a transmitter and an antenna). Practical waveguides are tipically rectangular or circular and, as prescribed by the electromagnetic theory [25], the electromagnetic field inside a waveguide travels in discrete transverse modes indexed by integers m and n. A mode converter is a microwave device capable of changing the propation mode of a field in a waveguide, and can be used for example to split the power between two loads.

We consider a TE_{10} to TE_{20} waveguide mode converter of the type studied in [40, Chapter 14] and depicted in Figure 15. We are interested in determining the TE_{10} reflection coefficient at the Port 1 (i.e. the S-parameter S_{11} [25]) of the structure in the frequency ranges between 7 and 11 GHz, where the mode conversion does not take place, and between 13 and 17 GHz, where mode conversion takes place (Figure 17). We compare our solution with the solution computed by a commercial multiphysics FEM package.

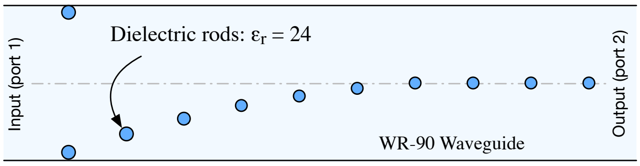

Figure 15: Structure of the simulated mode converter. The structure is built in a WR-90 waveguide and the dielectric rods (blue circles) have a relative permittivity $\epsilon_r = 24$. The input port is on the left (TE_{10} mode) and the output port is on the right (TE_{20} mode)

In the FEM model, the structure is terminated at both ends with Perfectly Matched Layers (PMLs) and excited with a waveguide port, as an impedance boundary condition equivalent to the one used for HHO is not available in the FEM package. On the other hand, in our HHO model we use an impedance boundary condition to terminate the structure: on the left side the impedance condition is matched to the wave impedance of the TE_{10} mode, whereas on the right side the termination is matched to the impedance of the output mode. The reason why we do not employ PMLs in HHO is that their development requires a better understanding of the HHO behaviour when complex wavenumbers appear. Indeed, as observed also with the HDG method [29], HHO too appears to not behave entirely as expected in this setting. To the best of our knowledge however, the HDG receipt [29] seems to not be straightforwardly applicable to HHO, therefore more investigation (which we will leave for a future contribution) is needed in this area.

The FEM mesh is composed of tetrahedral elements, whereas the HHO mesh is composed – in order to put in evidence the polyhedral nature of HHO – by a single layer of triangular prisms. In both the FEM and HHO models the amplitude of the reflected field is evaluated by exploiting the orthogonality between modes [31, Section 5.1.3] as

$$a_{\mathrm{TE}_{10}} := \frac{\int_\Gamma (\boldsymbol{e} - \boldsymbol{e}_{10}) \cdot \boldsymbol{e}_{10} \, \mathrm{d}\Gamma}{\int_\Gamma \boldsymbol{e}_{10} \cdot \boldsymbol{e}_{10} \, \mathrm{d}\Gamma}, \tag{17}$$

where Γ is the interface corresponding to Port 1 (Figure 15), $\boldsymbol{e}$ is the computed total field on Γ and $\boldsymbol{e}_{10}$ is the excitation applied on Γ. The amplitude is then used to compute the return loss S_{11} in decibels (Figure 16). In both regimes we observe a good match between the FEM solution and the HHO solution; the slight differences, negligible in practice, can be attributed to the slightly different models we employed.

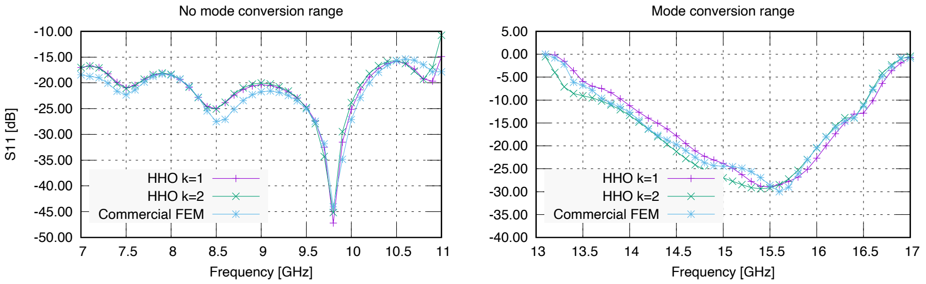

Figure 16: On the left the computed return loss between 7 and 11 GHz, where the mode conversion does not take place. On the right the computed return loss as TE_{10} mode between 13 and 17 GHz, where a TE_{10} to TE_{20} mode conversion takes place.

8 Conclusions

We introduced a numerical method for the indefinite time-harmonic Maxwell problem inspired on the design philosophy of the original HHO method for elliptic problems, and we evaluated experimentally its computational performance against the classical SIP-DG method. As expected from hybrid methods, HHO requires far less computational effort than SIP-DG, which is an important advantage on the solution of the indefinite time-harmonic Maxwell problem. More importantly, HHO also helps in reducing the quantity of memory required by the linear solver when compared to SIP-DG.

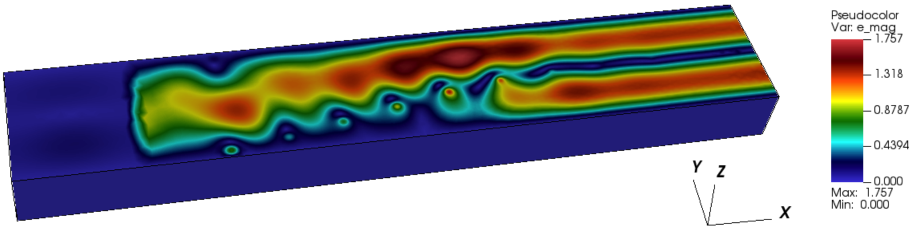

Figure 17: Field pattern at 15.5 GHz. From the left to right one can observe the scattered field region, the TF/SF transition where the excitation is applied and the total field region, where the mode conversion takes place. The left end is terminated with the impedance of the TE_{10} mode, whereas right end is terminated with the impedance of the TE_{20} mode.

Subsequently we described the HHO realization of two important tools, namely a plane wave boundary condition and a total field/scattered field decomposition, which we validated obtaining the expected convergence of the considered quantities.

As a more real-world problem, we presented the study of a waveguide mode converter and we compared our results with those obtained from a commercial code. Satisfactory agreement was found.

There are many aspects of the method that still need to be understood, we leave deeper theoretical studies, as well as the introduction of other important numerical tools such as the PMLs, for a future contribution.

9 Acknowledgements

The authors wish to express their gratitude to S. Lemaire (INRIA), Z. Dong (INRIA) and T. Chaumont-Frelet (INRIA) for the useful discussions about some of the theoretical aspects of the HHO method.

References

[1] M. Abbas, A. Ern, and N. Pignet. Hybrid High-Order methods for finite deformations of hyperelastic materials. *Comput. Mech.*, 62(4):909–928, 2018.

[2] M. Abbas, A. Ern, and N. Pignet. A Hybrid High-Order method for incremental associative plasticity with small deformations. *Comput. Methods Appl. Mech. Engrg.*, 346:891–912, 2019.

[3] M. Abbas, A. Ern, and N. Pignet. A Hybrid High-Order method for finite elastoplastic deformations within a logarithmic strain framework. *Internat. J. Numer. Methods Engrg.*, 120(3):303–327, 2019.

[4] Ayuso de Dios, Blanca, Lipnikov, Konstantin, and Manzini, Gianmarco. The nonconforming virtual element method. *ESAIM: M2AN*, 50(3):879–904, 2016.

[5] E. Burman, G. Delay, and A. Ern. An unfitted hybrid high-order method for the Stokes interface problem. *IMA J. Numer. Anal.*, 2021. hal-02280426.

[6] E. Burman, O. Duran, and A. Ern. Hybrid high-order methods for the acoustic wave equation in the time domain. *Commun. Appl. Math. Comput.*, 2021. hal-02922702.

[7] E. Burman, O. Duran, A. Ern, and M. Steins. Convergence analysis of hybrid high-order methods for the wave equation. *J. Sci. Comput.*, 87(3):Paper No. 91, 30, 2021.

[8] Erik Burman, Matteo Cicuttin, Guillaume Delay, and Alexandre Ern. An unfitted hybrid high-order method with cell agglomeration for elliptic interface problems. 43(2):A859 – A882, 2021.

[9] L. Camargo, B. López-Rodríguez, M. Osorio, and M. Solano. An HDG method for Maxwell's equations in heterogeneous media. *Computer Methods in Applied Mechanics and Engineering*, 368:113178, 2020.

[10] K. L. Cascavita, J. Bleyer, X. Chateau, and A. Ern. Hybrid discretization methods with adaptive yield surface detection for Bingham pipe flows. *J. Sci. Comput.*, 77(3):1424–1443, 2018.

[11] K. L. Cascavita, F. Chouly, and A. Ern. Hybrid high-order discretizations combined with Nitsche's method for Dirichlet and Signorini boundary conditions. *IMA J. Numer. Anal.*, 40(4):2189–2226, 2020.

[12] F. Chave, D. A. Di Pietro, and S. Lemaire. A discrete Weber inequality on three-dimensional hybrid spaces with application to the HHO approximation of magnetostatics. *Mathematical Models and Methods in Applied Sciences*, 32(01):175–207, 2022.

[13] Huangxin Chen, Weifeng Qiu, Ke Shi, and Manuel Solano. A Superconvergent HDG Method for the Maxwell Equations. *Journal of Scientific Computing*, 70(3):1010–1029, 2017.

[14] S. Chialina, M. Cicuttin, L. Codecasa, R. Specogna, and F. Trevisan. Plane wave excitation for frequency domain electromagnetic problems by means of impedance boundary condition. *IEEE Trans. Magn*, 51(3), 2015.

[15] M. Cicuttin, L. Codecasa, R. Specogna, and F. Trevisan. Complementary Discrete Geometric h -Field Formulation for Wave Propagation Problems. *IEEE Transactions on Magnetics*, 52(3):1–4, 2016.

[16] M. Cicuttin, L. Codecasa, R. Specogna, and F. Trevisan. Excitation by Scattering/Total Field Decomposition and Uniaxial PML in the Geometric Formulation. *IEEE Trans. Magn*, 52(3), 2016.

[17] M. Cicuttin, L. Codecasa, R. Specogna, and F. Trevisan. A geometric frequency-domain wave propagation formulation for fast convergence of iterative solvers. *IEEE Trans. Magn*, 53(6), 2017.

[18] M. Cicuttin, D. A. Di Pietro, and A. Ern. Implementation of Discontinuous Skeletal methods on arbitrary-dimensional, polytopal meshes using generic programming. *J. Comput. Appl. Math.*, 344:852–874, 2018.

[19] M. Cicuttin, A. Ern, and T. Gudi. Hybrid high-order methods for the elliptic obstacle problem. *J. Sci. Comput.*, 83(1):Paper No. 8, 18, 2020.

[20] M. Cicuttin, A. Ern, and N. Pignet. *Hybrid High-Order Methods. A primer with applications to Solid Mechanics.* SpringerBriefs in Mathematics. Springer, 2021.

[21] B. Cockburn, D. A. Di Pietro, and A. Ern. Bridging the Hybrid High-Order and Hybridizable Discontinuous Galerkin Methods. *ESAIM: Mathematical Modelling and Numerical Analysis*, 50, 2015.

[22] B. Cockburn, J. Gopalakrishnan, and R. Lazarov. Unified hybridization of discontinuous Galerkin, mixed, and continuous Galerkin methods for second order elliptic problems. *SIAM J. Numer. Anal.*, 47(2):1319–1365, 2009.

[23] B. Cockburn, J. Gopalakrishnan, and F.-J. Sayas. A projection-based error analysis of HDG methods. *Math. Comp.*, 79(271):1351–1367, 2010.

[24] Bernardo Cockburn. *Static Condensation, Hybridization, and the Devising of the HDG Methods*, pages 129–177. Springer International Publishing, Cham, 2016.

[25] R. E. Collin. *Foundations for Microwave Engineering.* Wiley, 2001.

[26] D. A. Di Pietro and A. Ern. A Hybrid High-Order locking-free method for linear elasticity on general meshes. *Comput. Meth. Appl. Mech. Engrg.*, 283:1–21, 2015.

[27] D. A. Di Pietro, A. Ern, and S. Lemaire. An arbitrary-order and compact-stencil discretization of diffusion on general meshes based on local reconstruction operators. *Comput. Meth. Appl. Math.*, 14(4):461–472, 2014.

[28] Robert Eymard, Gérard Henry, Raphaèle Herbin, Florence Hubert, Robert Klöfkorn, and Gianmarco Manzini. 3d benchmark on discretization schemes for anisotropic diffusion problems on general grids. In Jaroslav Fořt, Jiří Fürst, Jan Halama, Raphaèle Herbin, and Florence Hubert, editors, *Finite Volumes for Complex Applications VI Problems & Perspectives*, pages 895–930, Berlin, Heidelberg, 2011. Springer Berlin Heidelberg.

[29] J. Gopalakrishnan, S. Lanteri, N. Olivares, and R. Perrussel. Stabilization in relation to wavenumber in HDG methods. *Advanced Modeling and Simulation in Engineering Sciences*, 2, 2015.

[30] P. Houston, I. Perugia, A. Schneebeli, and D. Schoetzau. Interior penalty method for the indefinite time-harmonic Maxwell equations. *Numerische Mathematik*, 100:485–518, 2005.

[31] J. Jin and D. J. Riley. *Finite Element Analysis of Antennas and Arrays.* Wiley, 2009.

[32] L. Li, S. Lanteri, N. Asger Mortensen, and M. Wubs. A hybridizable discontinuous Galerkin method for solving nonlocal optical response models. *Computer Physics Communications*, 219:99–107, 2017.

[33] L. Li, S. Lanteri, and R. Perrussel. Numerical investigation of a high order hybridizable discontinuous galerkin method for 2d time-harmonic maxwell's equations. *COMPEL - The international journal for computation and mathematics in electrical and electronic engineering*, 32, 2013.

[34] M. Lin, W. Junping, Y. Xiu, and Shangyou. Z. A weak galerkin finite element method for the maxwell equations. *J. Sci. Comp.*, 65:363–386, 2015.

[35] R. G. Marchand, M. M. Botha, and D. B. Davidson. Total and Scattered Field Decomposition for the Vector Helmoholtz Equation Using the FETI. *Electromagnetics*, 28:77–91, 2008.

[36] G. Nehmetallah, S. Lanteri, S. Descombes, and A. Christophe. An Explicit Hybridizable Discontinuous Galerkin Method for the 3D Time-Domain Maxwell Equations. In Spencer J. Sherwin, David Moxey, Joaquim Peiró, Peter E. Vincent, and Christoph Schwab, editors, *Spectral and High Order Methods for Partial Differential Equations ICOSAHOM 2018*, pages 513–523, Cham, 2020. Springer International Publishing.

[37] N.C. Nguyen, J. Peraire, and B. Cockburn. Hybridizable discontinuous Galerkin methods for the time-harmonic Maxwell's equations. *Journal of Computational Physics*, 230(19):7151–7175, 2011.

[38] D. J. Riley, J. Jin, Z. Lou, and L. E. R. Petersson. Total-and Scattered-Field Decomposition Technique for the Finite-Element Time-domain Method. *IEEE Trans. Ant. Prop*, 54(1), 2006.

[39] J. Wang and X. Ye. A weak Galerkin finite element method for second-order elliptic problems. *J. Comput. Appl. Math.*, 241:103–115, 2013.

[40] V. Zhurbenko, editor. *Electromagnetic Waves.* InTech, Rijeka, Croatia, 2011.